AIAA-2000-0437

Ignition and Flame Studies for an Accelerating Transonic Mixing Layer

X. Fang, F. Liu, and W. A. Sirignano
University of California, Irvine
Irvine, CA 92697-3975

38th Aerospace Sciences Meeting & Exhibit
10-13 January 2000 / Reno, NV

Ignition and Flame Studies for an Accelerating Transonic Mixing Layer

X. Fang*, F. Liu†, W. A. Sirignano‡
Department of Mechanical and Aerospace Engineering
University of California, Irvine, CA 92697-3975

Numerical solutions have been obtained for a diffusion flame in the two-dimensional, laminar, steady, viscous, multicomponent, compressible mixing layer in the presence of a pressure gradient by using the boundary layer approximations and solving the $x-$momentum, energy, and species conservation equations. The numerical solutions have been validated against similarity solutions, and then are extended to cases where no similarity solution exists. The numerical solutions are used to study the ignition process and the flame structure in an accelerating transonic mixing layer. It is shown how ignition length depends upon initial temperature, initial pressure, initial velocity, transport properties, and pressure gradient. Ignition is found to occur on the high-temperature air side. Oxidation kinetics and transport are both controlling in the upstream ignition region. Further downstream, transport is controlling in the fully established flame. The boundary layer approximation is found to be valid everywhere including the upstream ignition region.

Nomenclature

c_p	specific heat
D	mass diffusivity
h	enthalpy
H	stagnation enthalpy
H_s	sensible stagnation enthalpy
h_t	total enthalpy
h^o	heat of formation
K	the ratio of the freestream velocities $u_\infty/u_{-\infty}$
M	Mach number
N	total number of species
Pr	Prandtl number
p	pressure
R	gas constant
Sc	Schmidt number
T	temperature
u_∞	dimensional freestream velocity (characteristic velocity)
$u_{-\infty}$	dimensional freestream velocity
u	velocity in x-direction
v	velocity in y-direction
W	molecular weight
x, y	Cartesian coordinates
x_{ch}	chemical distance, $\frac{\rho u}{Ae^{-E_a/RT}[Fuel]^a[O_2]^b}$
Y_i	mass fraction
Z	Schvab-Zel'dovich variable

Greek symbols

β_M	acceleration parameter
η	similarity variable
λ	thermal conductivity
μ	coefficient of viscosity
$\dot{\omega}$	reaction rate
ρ	density
ξ	similarity variable
ν	stoichiometric coefficient

Subscript

F	fuel
i	species (O_2, N_2, H_2O, CO_2, or CH_4)
j	species (air or fuel)
∞	quantity at the top far away from the layer
$-\infty$	quantity at the bottom far away from the layer
ref	quantity at reference condition
ig	ignition

*Graduate Student Researcher.

†Associate Professor of Mechanical and Aerospace Engineering, Senior member AIAA.

‡Professor of Mechanical and Aerospace Engineering, Fellow AIAA.

1 Introduction

The objective of this study is to analyze some of the issues related to a new technology concerned with the acceleration of reacting flows. One application concerns gas turbine engines; designers are attempting to increase the thrust-to-weight ratio and to widen the range of engine operation. One major consequence is that the combustor residence time can become shorter

than the time required to complete combustion. Therefore, combustion would occur in the turbine passage. A significant benefit can result from augmented burning in the turbine. Sirignano and Liu [1, 2] have shown by thermodynamic analysis that augmented combustion in the aircraft turbojet engine allows for (1) a reduction in after-burner length and weight, (2) a reduction in specific fuel consumption, and (3) an increase in specific thrust. The increase in specific thrust implies that larger thrust can be achieved with the same cross-section or that the same thrust can be achieved with a smaller cross-section (and therefore still smaller weight). For the ground-based gas turbine, benefits have been shown by thermodynamic analysis to occur in power/weight and efficiencies [1]. A mixing and exothermic chemical reaction in the accelerating flow through the turbine passage offers, therefore, an opportunity for a major technological improvement. The gas turbine engine is not the only potential application for this technology. The reduction in peak temperatures due to acceleration results in the promise of reduced pollutant formation and reduced heat transfer losses in many other combustion applications.

There is a lack of fundamental treatment in the literature of multidimensional flows with mixing and chemical reaction in the presence of strong pressure gradients that support a transonic flow. For zero pressure gradients, reacting, multi-dimensional (laminar and turbulent) low Mach number mixing and boundary layer flows have been considered by many investigators using a wide variety of approaches. See, for example, Marble and Adamson [3], Emmons [4], Chung [5], and Sharma and Sirignano [6] for laminar flows, and Patankar and Spalding [7], Razdan and Kuo [8], and Givi et al. [9], for turbulent flows. A limited number of efforts have been made on reacting supersonic flows. See, for example, Buckmaster et al. [10], Grosch and Jackson [11], Jackson and Hussaini [12], Im et al. [13, 14], and Chakraborty et al. [15]. For a two-dimensional, laminar, nonreacting, boundary layer over a solid body with a pressure gradient, similarity solutions were obtained by Li and Nagamatsu [16], Cohen [17], and Cohen and Reshotko [18] who solved the momentum and energy equations transformed by the Illingworth-Stewartson transformation (Illingworth [19], Stewartson [20], Schlichting [21]).

Sirignano and Kim [22] reduced the partial differential equations to a system of ordinary differential equations, and obtained similarity solutions for laminar, two-dimensional, mixing, reacting and nonreacting layers with a pressure gradient that accelerates the flow in the direction of the primary stream.

These similarity solutions offer some insight into the effect of flow acceleration on the flame structure in the mixing layer. However, they are only valid for restricted classes of flows with certain particular pressure gradients. Moreover, it is not capable to predict the ignition process close to the trailing edge of the splitter plate. In this paper, we develop a finite-difference method for solving the two-dimensional mixing layer equations with chemical reaction without the use of the similarity assumption. We will first compare computational results with the similarity solutions obtained by Sirignano and Kim [22], and then extend our computations to non-similar cases in order to examine the ignition and combustion processes in a general transonic accelerating mixing layer.

2 Governing Equations

Consider a diffusion flame in the two-dimensional, laminar, steady, viscous, multicomponent, compressible mixing layer in the presence of a pressure gradient. At the trailing edge of a flat splitter plate, the hot air mixed with burned gases flowing above the flat plate at the velocity u_∞ comes into contact with a fuel vapor flowing below the flat plate at the velocity $u_{-\infty}$. Then, a chemical reaction takes place between the air and the fuel vapor, and a diffusion flame will be established near the middle of the shear layer.

We are concerned with the ignition and combustion that is established downstream of the point of initial contact between the fuel and air streams.

After use of the boundary layer approximations and replacement of the pressure term in the $x-$momentum equation by the term involving freestream velocity, i.e.,

$$\rho_\infty u_\infty \frac{du_\infty}{dx} = \rho_{-\infty} u_{-\infty} \frac{du_{-\infty}}{dx} = -\frac{dp}{dx} \tag{1}$$

we can write the $x-$momentum, energy, and species conservation equations as:

$$\begin{aligned} \frac{\partial}{\partial x}\left(\frac{u}{u_\infty}\right) &= -\frac{v}{u}\frac{\partial}{\partial y}\left(\frac{u}{u_\infty}\right) + \frac{1}{\rho u}\frac{\partial}{\partial y}\left[\mu \frac{\partial(\frac{u}{u_\infty})}{\partial y}\right] \\ &\quad + \frac{1}{u}\left[\frac{\rho_\infty}{\rho} - \left(\frac{u}{u_\infty}\right)^2\right]\frac{du_\infty}{dx} \end{aligned} \tag{2}$$

$$\begin{aligned} \frac{\partial H}{\partial x} &= -\frac{v}{u}\frac{\partial H}{\partial y} + \frac{1}{\rho u Pr}\frac{\partial}{\partial y}\left(\mu \frac{\partial H}{\partial y}\right) \\ &\quad + \frac{1}{\rho u}\left(\frac{1}{Sc} - \frac{1}{Pr}\right)\frac{\partial}{\partial y}\left(\mu \sum_{i=1}^{N} h_{t,i}\frac{\partial Y_i}{\partial y}\right) \\ &\quad + \frac{1}{\rho u}\left(1 - \frac{1}{Pr}\right)\frac{\partial}{\partial y}\left[\mu \frac{\partial(\frac{u^2}{2})}{\partial y}\right] \end{aligned} \tag{3}$$

$$\frac{\partial Z_j}{\partial x} = -\frac{v}{u}\frac{\partial Z_j}{\partial y} + \frac{1}{\rho u Sc}\frac{\partial}{\partial y}\left(\mu\frac{\partial Z_j}{\partial y}\right), \qquad j = 1, 2 \quad (4)$$

$$\frac{\partial Y_F}{\partial x} = -\frac{v}{u}\frac{\partial Y_F}{\partial y} + \frac{1}{\rho u Sc}\frac{\partial}{\partial y}\left(\mu\frac{\partial Y_F}{\partial y}\right) + \frac{\dot{\omega_F}}{\rho u} \quad (5)$$

where i denotes O_2, N_2, H_2O, CO_2, and CH_4. The reaction rate $\dot{\omega}_j$ in the species equation has been eliminated by introducing the Schvab-Zel'dovich variables:

$$Z_j = Y_j - \nu_j Y_F, \qquad j = 1, 2. \quad (6)$$

where $j = 1$ denotes air, $j = 2$ denotes products.

The Prandtl number is defined as

$$Pr = \frac{c_p \mu}{\lambda} \quad (7)$$

where λ is thermal conductivity. The Schmidt number is defined as

$$Sc = \frac{c_p \mu}{D} \quad (8)$$

where D is mass diffusivity.

The stagnation enthalpy is defined as

$$H = h_t + \frac{1}{2}u^2 \quad (9)$$

and the total enthalpy is

$$h_t = \int_{T_{ref}}^{T} c_p dT' + \sum_{i=1}^{N} Y_i h_i^o \quad (10)$$

where h_i^o is the heat of formation of species i at the reference temperature T_{ref}.

The boundary conditions are specified as below:
$u \longrightarrow u_\infty$, $H \longrightarrow H_\infty$, $Z_j \longrightarrow Z_{j\infty}$, as $y \longrightarrow \infty$;
$u \longrightarrow u_{-\infty}$, $H \longrightarrow H_{-\infty}$, $Z_j \longrightarrow Z_{j-\infty}$ as $y \longrightarrow -\infty$.

A perfect gas is assumed

$$p = \sum_{i=1}^{N} \rho Y_i R_i T \quad (11)$$

In the solution procedure, the average gas constant R, molecular weight W, viscosity coefficient μ can be obtained by the following equations:

$$R = \sum_{i=1}^{N} R_i Y_i \quad (12)$$

$$\frac{1}{W} = \sum_{i=1}^{N} \frac{1}{W_i} Y_i \quad (13)$$

$$\mu = \sum_{i=1}^{N} \mu_i(T) Y_i. \quad (14)$$

The viscosity coefficient of each species μ_i is obtained by using Sutherland-law [23]:

$$\frac{\mu_i}{\mu_0} = (T/T_0)^{\frac{3}{2}} \frac{T_0 + S}{T + S} \quad (15)$$

3 Solution Methods and Constraints

We consider steady, two-dimensional, compressible flow. Pr and Sc are constant in each case, but they can vary from case to case. In this calculation, we solve five equations, one for the dimensionless velocity u/u_∞, two for the Schvab-Zel'dovich variables Z_{air} and $Z_{product}$, one for the fuel mass fraction Y_F, one for the stagnation enthalpy H.

We have developed a two-dimensional, implicit, finite-difference algorithm to solve simultaneously the set of the discretized partial differential equations. The method is based on the Crank-Nicolson [24] scheme. It is second-order accurate in both the x-direction and the y-direction.

We first solve for velocity in x-direction u, temperature T, and mass fractions of all the species from Equation (2), (3), and (5), respectively, by using parameters in the previous step. Then we calculate density ρ and velocity in y-direction v from equation of state and continuity equation respectively using the new solutions. After the solutions at this step have been obtained, we use the mean value of parameters at this step and the previous step in the next iteration and solve the set of partial differential equations again. We compare the new solutions and the last solutions to see if they are accurate enough. Our accuracy criteria is that the difference between the last two solutions in fuel mass fraction at any grid point in y direction must be less than 1.0×10^{-6} and in temperature must be less than 1.0×10^{-3} K. If both conditions are satisfied, we go to the next x step, otherwise we iterate again. Normally each step needs 6-10 iterations to satisfy the accuracy criteria.

The momentum balance in the y direction can be expressed as:

$$\rho_\infty u_\infty v_\infty = -\rho_{-\infty} u_{-\infty} v_{-\infty} \quad (16)$$

After u has been solved from Equation (2), v can be obtained by integrating the continuity equation,

$$\rho v = \rho_{-\infty} v_{-\infty} - \int_{-\infty}^{y} \frac{\partial(\rho u)}{\partial x} dy'. \quad (17)$$

After H has been solved from Equation (3), we can calculate temperature by using the following equations:

$$h = \sum_{i=1}^{N} h_i Y_i = \int_{T_{ref}}^{T} \sum_{i=1}^{N} c_{p_i} Y_i dT' \quad (18)$$

$$h = H - \frac{1}{2}u^2 - \sum_{i=1}^{N} Y_i h_i^o \quad (19)$$

$$dh = \sum_{i=1}^{N} h_i dY_i + \sum_{i=1}^{N} c_{p_i} Y_i dT. \quad (20)$$

where,

$$c_p = \sum_{i=1}^{N} c_{p_i}(T) Y_i \quad (21)$$

Equation (18) can be rewritten as:

$$dh = \sum_{i=1}^{N} h_i dY_i + c_p dT, \quad (22)$$

from which dT can be solved, and thus temperature can be calculated at each point in space.

Methane (CH_4) is used for the current computations although the method is not restricted to only one type of fuel. The combustion process is described by a one-step overall chemical reaction as:

$CH_4 + 2O_2 + 7.52N_2 \quad \longrightarrow CO_2 + 2H_2O + 7.52N_2$

The chemical kinetics rate can be described as:

$$\dot{\omega_F} = Ae^{-E_a/RT}[Fuel]^a[O_2]^b \quad (23)$$

where [] represents molar concentration in mol/cm^3. According to [25] for methane (CH_4), $A = 2.8 \times 10^9$ 1/second, $E_a = 48.4$ kcal/mol, $a = -0.3$, $b = 1.3$. Note that the kinetic time will be independent of pressure for these values.

4 Comparison with Similarity Solutions

Sirignano and Kim [22] obtained similarity solutions for a laminar, two-dimensional, mixing, reacting and non-reacting layers with certain prescribed pressure gradients. In this section, we calculate the same similarity cases using the new finite-difference method without the similarity assumptions. After obtaining the flow field, the solution are recast in the same similarity variables and compared with the results by Sirignano and Kim [22].

Non-reacting single-component case. In this case the fluids below and above the splitter plate are both air but have different velocities and temperatures. Hot air flowing above the flat plate at the velocity u_∞ comes into contact with cold air flowing below the flat plate at the velocity $u_{-\infty}$. Similarity solutions exist for situations where K and β_M are constants [22]. Here, K is the ratio of the freestream velocities $u_\infty/u_{-\infty}$, and β_M is the acceleration parameter,

$$\beta_M = \beta(1 + \frac{\gamma - 1}{2} M_\infty^2) \quad (24)$$

M_∞ is the Mach number at the top freestream and

$$\beta(\overline{\xi}) = \frac{2\xi}{u_\infty} \frac{du_\infty}{d\overline{\xi}} \quad (25)$$

where $\overline{\xi}$ is a similarity variable

$$d\overline{\xi} = u_\infty d\xi \quad (26)$$

$$d\xi = \frac{\rho u}{\rho_0 u_0} dx \quad (27)$$

The subscript 0 refers to stagnation conditions in the freestream. $\beta_M > 0$ means accelerating, $\beta_M < 0$ means decelerating. We compare the solution of the system of PDEs with similarity solutions by Sirignano and Kim [22] for the dimensionless velocity u/u_∞ and the dimensionless sensible stagnation enthalpy $(H_s - H_{s-\infty})/H_{s\infty}$ under the conditions that $K = 5$ and $\beta_M = 1$. Figure 1 shows the dimensionless velocity u/u_∞ versus η. Figure 2 shows the dimensionless sensible stagnation enthalpy $(H_s - H_{s-\infty})/H_{s\infty}$ versus η. The close agreement between the numerical solutions and the similarity solutions verifies the accuracy of our computational code.

Reacting multi-component case. In this case, a hot air mixed with burned gases flowing above the flat plate at the velocity u_∞ comes into contact with a fuel vapor mixed with burned gases flowing below the flat plate at the velocity $u_{-\infty}$. Similarity solutions exist again for situations where K and β_M are constants [22] and the reaction rate is infinite.

In this section, we compare the dimensionless velocity u/u_∞ and the dimensionless sensible stagnation enthalpy $(H_s - H_{s-\infty})/H_{s\infty}$ under the conditions that $K = 1.623$ and $\beta_M = 2$. Figure 3 shows the dimensionless velocity u/u_∞ versus η. In the presence of accelerating pressure gradients, the maximum velocity occurs near the middle of the shear layer, where the temperature is high due to the chemical reaction and thus the density is low. The low density regime experiences the greatest acceleration. It is noted that the maximum velocity is lower in the solution of PDEs than in the similarity solution. In the similarity solution, the model of infinite chemical kinetics rate is used, while in the solution of PDEs, we use the actual chemical kinetics rate, which produces a lower peak temperature and a higher minimum density.

Figure 4 shows the temperature versus η at different $\overline{\xi}$ locations. At the same $\overline{\xi}$ position, the maximum temperature is lower in the solution of PDEs than in the similarity solution due to the use of finite rate chemistry. As $\overline{\xi}$ increases, the difference becomes more and more obvious because the actual chemical kinetics rate becomes lower and lower.

5 Non-similar Solutions

After validating our numerical method against the similarity solutions, we extend our calculation to cases where no similarity solution exists.

We consider the same reacting case as in Section 4 where a hot air at the velocity u_∞ comes into contact with a fuel vapor at the velocity $u_{-\infty}$. However, we will remove the similarity conditions that K and β_M are constants. We consider flows with arbitrary freestream velocities and pressure gradients and use finite-rate chemical kinetics where no similarity solution exists.

In this section we study the influence of various flow parameters on ignition and flame structure. Table 1 lists the different cases of study. Cases 1-13 represent a set of studies within which each flow parameter, including the initial air temperature, pressure and initial air fraction, varies independently relative to the base case (Case 1). In a practical application, however, the initial air fraction of the air/fuel mixture coming into the turbine has a dependence on the turbine inlet temperature and pressure since fuel is burned in the main combustor to reach the prescribed temperature. Consequently, the initial temperature or pressure in our studies cannot be realistically varied independently without changing the initial air mass fraction. Therefore, additional cases, Cases 14-17, are studied in which variation of initial temperature or pressure is accompanied by a corresponding variation in initial air mass fraction based on a combustion model for the main combustor of a jet engine. These cases will be referred to as the Coupled Cases and will be presented in Section 6. Results for Cases 1-13, the uncoupled studies, are presented in this section.

Base case. Figure 5 shows temperature contours under the base case (Case 1) parameters. From Figure 5 we can see that the ignition occurs after a certain distance in x direction. Figure 6 is a close-up view of the temperature contours near the ignition region. Figure 7 displays the temperature versus y at four different x positions. The peak value of the temperature and the two temperatures at the freestream locations decrease as one moves downstream. The flow accelerates due to the pressure gradient but the stagnation temperature remains the same; therefore the temperature will decrease in the downstream direction.

The peak value of the temperature occurs at a positive value of y (the air side) and is moving upward when the flow moves downstream. The reason is that the mass of air required in stoichiometric combustion is much greater than that of the fuel. Figure 8 shows the density ρ versus y at four different x positions for the base case. The density curve has a minimum point where the temperature is high whereas pressure is the same at the same x position. Figure 9 presents the dimensionless velocity u/u_∞ versus y at four different x positions for the base case. The boundary layer becomes thicker and the ratio $u_{-\infty}/u_\infty$ becomes larger as the flow moves downstream. At the air side both the density and the velocity are greater than at the fuel (CH_4) side. From the free stream momentum equation (1), the acceleration at the fuel (CH_4) side should be greater than the acceleration at the air side.

From Figure 8 the density near the middle of the shear layer is smaller than the density at two free streams, so under the same pressure gradient the acceleration is higher near the middle of the shear layer. Therefore the dimensionless velocity curve has a peak at the same y position as the density minimum point and the temperature peak. Figure 10 displays the mass fraction versus y at $x = 10.0$ cm for the base case. The peak value of the product mass fraction also occurs at a positive value of y. There is a peak for mass fraction of O_2 in Figure 10. It occurs because at some y positions the O_2 density due to diffusion is greater than the O_2 consumed by the chemical reaction, since at these positions the chemical reaction rate is low. Figure 11 shows the Mach number M versus y at four different x positions for the base case. The curve has a minimum point where the temperature peaks, since there the speed of sound is high and the Mach number is small. This behavior is also evident in Figure 12. We can see that there is a local minimum point for Mach number a little below the main minimum point. Near that point because the temperature is already high, as we move from the fuel side to the air side. So the speed of sound is also high, but the velocity increases more slowly than temperature, and the Mach number decreases near that point. At a certain point, the velocity begins to increase very fast, even faster than temperature, so the Mach number begins to increase. In the middle of the flame, the temperature is very high, the Mach Number decreases again and forms a minimum point. It is also noticed that in parts of the flow region, for example $x = 7.5$ cm, the flame region is subsonic while the freestreams are supersonic.

Figure 13 shows air consumption rate (integral of reaction rate of air over y in a fixed x position, unit is kg/sm^2) and the corresponding height of air which is consumed by reaction vs. x for Case 1. The air consumption rate has a maximum point where the reaction rate is the highest over the whole x range. The corresponding height of air shows the height of air that we must supply in order to make it react efficiently. It has a point where the slope is maximum that is at the same

x position as the maximum point in air consumption rate.

Figure 14 and 15 show the reaction rate and product mass fraction vs. y at four different x positions for Case 1. At the first two x positions the thickness of the reaction rate and the thickness of product mass fraction are comparable. At the last two x positions the thickness of the reaction rate does not change much, but the thickness of product mass fraction changes a lot due to diffusion. It is obvious that in the beginning, reaction rate and diffusion are both controlling and further downstream the diffusion is controlling.

We also calculated the ratio of the diffusion rate in the flow direction to the diffusion rate in the transverse direction. The absolute value generally is less than 0.1%, except near x = 1.75 mm at a few points, the maximum value goes up to 14%. It means that the boundary layer approximation is adequate everywhere, including the upstream ignition region.

Variation in pressure gradient. Figure 16 and 17 show temperature contours for $dp/dx = 0$ atm/m (Case 2), and $dp/dx = -350$ atm/m (Case 3) respectively. Other parameters remain the same as in the base case. From the plots, we can see that with the increase of the absolute value of the pressure gradient, the ignition distance increases. This results from the increase in flow acceleration with the increased pressure gradient. That may influence ignition distance in two aspects: (1) diffusion is less due to lower temperature, which in turn is due to higher velocity; (2) the time needed to reach a certain point downstream is shorter due to higher velocity.

We can also see that the highest temperature is lower in the case of higher pressure gradient and the flame thickness is decreasing with the increase of the absolute value of the pressure gradient. The temperature decreases due to higher velocity and at the same time less time for diffusion can also decrease flame thickness.

Ignition distance. There are many parameters which can influence the ignition process and flame structure, we introduce two dimensionless parameters $(-dp/dx)(1/p_0)x_{ch}$ and x_{ig}/x_0 (x_0 means ignition length at $dp/dx = 0$) to show some of the influences.

Chemical distance x_{ch} is calculated by using Equation (23) and the parameters at the initial upper freestream. Here, we define ignition distance as the distance from the flat plate to the first x grid point where the local peak temperature at that point differs from the local peak temperature at the next x grid point by greater than 3 K. It means the temperature begins to grow very fast at that location.

The dimensionless ignition parameter is varied by keeping p_0 and T_0 constant and changing dp/dx. Figure 18 shows the dimensionless ignition distance versus the dimensionless ignition parameter for $p_0 = 30$, 60, 200 atm/m and $T_0 = 2000$ K which correspond to Cases 1, 4, 5, and 6, respectively. Other parameters are the same as in the base case. The plots show that the dimensionless ignition distance x_{ig}/x_0 (x_0 means ignition at $dp/dx = 0$) increases monotonically with the increase of the dimensionless ignition parameter $(dp/dx)(1/p_0)x_{ch}$ in all cases.

Variation in initial pressure. Initial pressure also has significant influence on ignition process. Figure 19 and Figure 20 displays temperature contours for initial pressure $p_0 = 60$ atm (Case 4) and $p_0 = 200$ atm (Case 5), respectively. The plots indicate that the higher the initial pressure is, the thinner the mixing layer is. That happens because, when the initial pressure is high, the density is high, the kinematic viscosity $\nu = \mu/\rho$ is smaller, and flow diffuses slower. The dependence on intial pressure in Figure 18 is not monotonic. An increase to $p_0 = 60$ atm reduces generally the ignition distance while an increase to 200 atm lengthens that distance. Realize that the chemical rate is independent of the pressure for the chosen fuel. As pressure increases, the mass diffusivity decreases thereby inhibiting the onset of ignition by this effect alone. This appears to explain the increase in the ignition length as we vary an initial pressure of 30 atm to 60 atm. However, another opposite effect is that, for a given pressure gradient and initial velocity, increases in the initial pressure and density reduce the acceleration and velocity gradient. Therefore, the flow expansion and reduction of temperature are reduced. By this mechanism, ignition length can decrease. This effect apparently dominates as the pressure is increased to 200 atm.

Variation in initial temperature. Figure 21 presents temperature contours in the flow field for initial air temperature $T_{air} = 2000$ K (Case 6). Figure 22 shows temperature contours in the flow fields for initial fuel temperature $T_F = 700$ K (Case 7).

The most important influence is the ignition distance; the higher the initial temperature is, the shorter the ignition distance is. We can also see that the highest temperature and the thickness of the high temperature zone depends on the initial temperature too. When the initial temperature is higher, the value of the highest temperature is greater and the high temperature zone is thicker.

Variation in initial velocity. Figures 23 and 24 show temperature contours in the flow fields for initial air velocity $u_{air} = 100$ m/s (Case 8) and initial fuel velocity $u_F = 100$ m/s (Case 9).

When the initial air velocity u_{air} is increased, the ignition distance increases. An increase in the fuel velocity, however, results in faster diffusion of fuel vapor across the layer and reduces ignition length.

Variation in Prandtl number. Figure 25 shows temperature contours in the flow field for $Pr = 0.9$ (Case 10). The ignition distance is longer and the shear layer is thicker. When we decrease Pr and keep the viscosity coefficient the same, we implicitly increase the thermal conductivity λ. Ignition tends to occur on the air side where temperature is highest; so an increase in heat loss from that side tends to inhibit ignition.

Variation in Schmidt number. Figure 26 displays temperature contours in the flow field for $Sc = 0.9$ (Case 11). The ignition distance is shorter and the shear layer is thicker. When we decrease the Schmidt number Sc and keep the viscosity coefficient the same, we implicitly increase the mass diffusivity D, which is helpful to ignition since, in order to ignite, the fuel must diffuse across the layer.

Variation in viscosity coefficient. Figure 27 presents the temperature contours in the flow field when we decrease the viscosity coefficient μ by a factor of 5 (Case 12). The ignition distance is a little shorter and the shear layer is much thinner. When we decrease the viscosity coefficient, we decrease kinematic viscosity $\nu = \mu/\rho$, which is important to the thickness of the mixing layer.

Variation in chemical reaction rate. Figure 28 displays the temperature profiles in the flow field when we decrease the chemical reaction rate by a factor of 10 (Case 13). When chemical reaction rate is small, the ignition distance increases and the highest temperature is lower. In the ignition region, both chemical rate and diffusion are controlling phenomena. In the downstream region with a fully established flame, the diffusion is rate controlling.

6 Coupled Study

In this section, we will study the influence of different parameters in a coupled way. When the initial pressure or initial temperature varies, the initial air fraction in the air flow is also changed correspondingly.

Assume that the hot air mixed with burned gases flowing above the flat plate was produced by a chemical reaction of air and CH_4, which is compressed to the initial pressure 30 atm from the reference temperature 298 K and the reference pressure 1.0 atm. After the reaction, the temperature of the products is elevated to the initial temperature T_0. The combustion process of this reaction is described by a one-step overall chemical reaction as:

$$CH_4 + 2(1+x)O_2 + 7.52(1+x)N_2 \longrightarrow CO_2 + 2H_2O + 7.52(1+x)N_2 + 2xO_2$$

In the base case, corresponding to an initial temperature $T_0 = 1650$ K and an initial pressure $p_0 = 30$ atm, the initial air fraction is $Y_{air} = 0.5848$.

Figure 29 shows temperature contours for Case 14. From this figure and Figure 32, we can see that the highest temperature is lower compared with Figures 5 and 7, which are for the case with air fraction $Y_{air} = 1.0$, because the upper free stream air fraction decreases and so does the chemical reaction rate. Figure 30 shows the ignition process for Case 14. We can see that the ignition distance is longer; the reason is the same as mentioned above. Figure 31 shows the dimensionless velocity u/u_∞ versus y at four different x positions. They are similar to the case in which the air fraction is 1.0. But the peak value of u/u_∞ is much less than the peak value for Case 1 in which the upper free stream air fraction is 1.0. Figure 32 presents temperature versus y at four different x positions. The ignition is much slower and the peak temperature is much lower. Both are due to the slower chemical reaction rate. Figure 33 shows density versus y at four different x positions. As a result of lower peak temperature value compared with Case 1, the minimum density value is not as low as in Figure 8 for Case 1.

Figure 34 displays the mass fraction versus y at $x = 10.0$ cm for Case 14. The peak value of the product mass fraction also occurs at a positive value of y. Near that point O_2 and fuel mass fractions decrease fast. In this case, O_2 mass fraction does not decrease across the layer as fast as in Case 1, and there is no local minimum value as in Case 1 either. This is caused by slower chemical reaction rate due to low air fraction.

Variation in initial pressure. Initial pressure also has significant influence on ignition process. Figure 35 and Figure 36 show temperature contours for initial pressure $p_0 = 60$ atm (Case 15) and $p_0 = 200$ atm (Case 16) respectively. Assume that the hot air mixed with burned gases flowing above the flat plate was produced by a chemical reaction of air and CH_4, which is compressed to the specified initial pressure from the reference temperature 298 K and the reference pressure 1.0 atm. After the reaction, the temperature of the products is elevated to an initial air temperature of 1650 K. Corresponding to an initial pressure $p_0 = 60$ atm, the initial air fraction is $Y_{air} = 0.6625$, while corresponding to the initial pressure $p_0 = 200$ atm the initial air fraction is $Y_{air} = 0.8500$.

The plots indicate that the higher the initial pressure

is, the thinner the mixing layer is. When the initial pressure is high, the density is high, the viscosity $\nu = \mu/\rho$ is smaller, and the flow diffuses slower. The same two opposite mechanisms of reduced mass diffusivity and reduced acceleration and expansion that appeared in the uncoupled study do again cause a non-monotonic behavior for the ignition length. That length increases as the initial pressure is raised to 60 atm. Then it decreases as the pressure increases to 200 atm.

Variation in initial temperature. Figure 37 shows temperature contours for an initial air temperature $T_{air} =$ 2000 K (Case 17). In this case, corresponding to the initial temperature $T_0 = 2000$ K and initial pressure $p_0 = 30$ atm the initial air fraction is $Y_{air} = 0.5848$. The ignition distance is shorter than in Case 14. Although the initial air fraction is less in this case, the high air temperature helps the ignition. The ignition distance is still longer than that in Case 6 where the initial temperature is also 2000 K but air fraction in the freestream is 1.

7 Conclusion

Ignition and combustion processes in a transonic accelerating mixing layer have been studied by a finite-difference method. The method has been validated against similarity solutions and has been extended to non-similar solutions.

The ignition first takes place on the high temperature air side of the mixing layer. Fuel vapor must diffuse across the mixing layer to ignite. Any modification that increases the temperature, the fuel vapor concentration, or the residence time in the ignition region will decrease ignition length. Therefore, ignition length decreases as thermal conductivity decreases, as air velocity decreases, as mass diffusivity increases, as fuel velocity increases, or as initial temperature increases. Increased pressure gradient results in more rapid expansion and temperature reduction with an increase in the ignition length.

The effect of initial pressure on the ignition distance is more complex with two opposing effects. Mass diffusivity decreases while pressure increases. Flow acceleration rate also decreases, for a given pressure gradient with an increase in initial pressure and density. The former effect inhibits ignition while the latter enhances it thereby causing an non-monotonic dependence of the initial pressure. The upstream region where ignition occurs has two processes with comparable rates: oxidation kinetics and mass diffusion. The product layer and reaction zone have comparable thicknesses there. Further downstream, the flame is fully established and the diffusion layer thickness is much greater than the reaction zone thickness. Clearly, diffusion is rate controlling there. The boundary layer approximation is found to be adequate everywhere, including the upstream ignition region. That is, diffusion rates in the flow direction is found to be generally negligible compared to transverse diffusion rates.

The results for the coupled and the uncoupled studies are in quantitative agreement. The effect of initial pressure for methane study should not be generalized since with the methane one-step kinetics, the reaction is of order unity. The laminar mixing layer thickness in these studies are typically sub-millimeter in size. More practical configurations are expected to be turbulent with much thicker layers as a consequence.

In the presence of accelerating pressure gradients, the maximum velocity and temperature occur near the middle of the shear layer. It is possible that, in an accelerating flow, the flame region is subsonic while the freestreams are supersonic.

The acceleration results in decreasing flame temperature with downstream distance. The analysis leads to the conclusion that substantial potential exists for the reduction of NO_x formation and decreases in heat transfer losses due to the peak temperature reduction. Extinction also becomes possible in some cases. Since we use the actual finite chemical kinetics, it is possible to explore pollutant formations or extinction in the future.

The plan for future work includes introduction of multi-step chemical reaction rate, turbulent flow, and the removal of the boundary layer approximation.

Acknowledgments

The authors thank the National Science Foundation for its support for this research under grant number CTS-9714930. The grant manager is Dr. Farley Fisher.

References

[1] W. A. Sirignano and F. Liu, "Performance Increases for Gas-Turbine Engines Through Combustion Inside the Turbine," *Journal of Propulsion and Power* 15, 1, pp. 111-118 (1999).

[2] F. Liu and W. A. Sirignano, "Turbojet and Turbofan Engine Performance Increases through Turbine Burners," *AIAA* paper-0741 (2000).

[3] F. E. Marble and T. C. Adamson, Jr., "Ignition and Combustion in a Laminar Mixing Zone," *Jet Propulsion* 24, 85 (1954).

[4] H. W. Emmons, "Thin Film Combustion of Liquid Fuel," *Z. Angew. Math. Mech.* 36, 60 (1956).

[5] P. M. Chung, "Chemically Reacting Nonequillibrium Boundary Layers," *Advances in Heat Transfer*, edited by J. P. Hartnett and T. F. Irvine, Jr. Academic Press, New York, pp. 109-270 (1965).

[6] O. P. Sharma and W. A. Sirignano, "On the Ignition of a Pre-mixed Fuel by a Hot Projectile," *Combust. Sci. Technol.* 1, pp. 481-494 (1970).

[7] S. V. Patankar and D. B. Spalding, *Heat and Mass Transfer in Boundary Layers* Intertext, London (1970).

[8] M. K. Razdan and K. K. Kuo, "Erosive Burning Study of Composite Solid Propellants by Turbulent Boundary-layer Approach," *AIAA J.* 17, 1225 (1979).

[9] P. Givi, J. I. Ramos, and W. A. Sirignano, "Probability Density Function Calculations in Turbulent Chemically Reacting Round Jets, Mixing Layers and One-dimensional Reactors," *J. Non-Equilib. Thermodyn.* 10, pp. 75-104 (1985).

[10] J. Buckmaster, T. L. Jackson, and A. Kumar, in *Combustion in High- Speed Flows* Kluwer Academic, Dordrecht, The Netherlands (1994).

[11] C. E. Grosch and T. L. Jackson, "Ignition and Structure of a Laminar Diffusion Flame in a Compressible Mixing Layer with Finite Rate Chemistry," *Phys. Fluids* A 3, pp. 3087-97 (1991).

[12] T. L. Jackson and M. Y. Hussaini, "An Asymptotic Analysis of Supersonic Reacting Mixing Layers," *Combust. Sci. Technol.* 57, 129 (1988).

[13] H. G. Im, B. H. Chao, J. K. Bechtold, and C. K. Law, "Analysis of Thermal Ignition in the Supersonic Mixing Layer," *AIAA J.* 32, pp. 341-9 (1994).

[14] H. G. Im, B. T. Helenbrook, S. R. Lee, and C. K. Law, "Ignition in the Supersonic Hydrogen/Air Mixing Layer with Reduced Reaction Mechanisms," *J. Fluid Mech.* 322, pp. 275-96 (1996).

[15] Chakraborty, D. and Upadhyaya, H.V.N. and Paul, P.J. and Mukunda, H.S. "A Thermo-chemical Exploration of a Two-dimensional Reacting Supersonic Mixing Layer," *Physics of Fluids* 9, 11, pp. 3513-22 (1997).

[16] T. Y. Li and H. T. Nagamatsu, "Similar Solutions of Compressible Boundary Layer Equations," *J. Aeronaut. Sci.* 20, 653 (1953).

[17] C. B. Cohen "Similar Solutions of Compressible Laminar Boundary Layer Equations," *J. Aeronaut. Sci.* 21, 281 (1954).

[18] C. B. Cohen and E. Reshotko, "The Compressible Laminar Boundary Layer with Heat Transfer and Arbitrary Pressure Gradient," *NACA Rep.* 1294, (1956).

[19] C. R. Illingworth "Steady Flow in the Laminar Boundary Layer of a Gas," *Proc. R. Soc.* London, Ser. A 199, 533 (1949).

[20] K. Stewartson, "Correlated Compressible and Incompressible Boundary Layers," *Proc. R. Soc.* London, Ser. A 200, 84 (1949).

[21] H. Schlichting, *Boundary Layer Theory* McGraw-Hill, New York, pp. 340-352 (1979).

[22] W. A. Sirignano and I. Kim "Diffusion Flame in a Two-dimensional, Accelerating Mixing Layer," *Physics of Fluids* 9, 9, pp. 2617-2630, (1997).

[23] Frank M. White *Viscous Fluid Flow*, 2nd edition, McGraw-Hill, Inc. (1991).

[24] C. A. J Fletcher *Computational Techniques for Fluid Dynamics* 2nd edition, Springer (1990).

[25] C. K. Westbrook and F. L. Dryer, "Chemical Kinetic Modeling of Hydrocarbon Combustion," *Prog. Energy Combust. Sci.* 10, pp. 1-57 (1984).

Case	T_{air} (K)	T_F (K)	p_0 (atm)	dp/dx (atm/m)	Y_{air}	u_{air} (m/s)	u_F (m/s)	Pr	Sc	$\dot{\omega}$ $(kg/m^3 s)$	μ (Ns/m^2)	x_{ig} (mm)
1	1650	400	30	−200	1.0	50	25	1.0	1.0	1.0	1.0	0.448
2	1650	400	30	0	1.0	50	25	1.0	1.0	1.0	1.0	0.416
3	1650	400	30	−350	1.0	50	25	1.0	1.0	1.0	1.0	0.496
4	1650	400	60	−200	1.0	50	25	1.0	1.0	1.0	1.0	0.656
5	1650	400	200	−200	1.0	50	25	1.0	1.0	1.0	1.0	0.384
6	2000	400	30	−200	1.0	50	25	1.0	1.0	1.0	1.0	0.064
7	1650	700	30	−200	1.0	50	25	1.0	1.0	1.0	1.0	3.200
8	1650	400	30	−200	1.0	100	25	1.0	1.0	1.0	1.0	3.440
9	1650	400	30	−200	1.0	50	100	1.0	1.0	1.0	1.0	0.080
10	1650	400	30	−200	1.0	50	25	0.9	1.0	1.0	1.0	1.280
11	1650	400	30	−200	1.0	50	25	1.0	0.9	1.0	1.0	0.064
12	1650	400	30	−200	1.0	50	25	1.0	1.0	1.0	0.2	0.080
13	1650	400	30	−200	1.0	50	25	1.0	1.0	0.1	1.0	0.432
14	1650	400	30	−200	0.5848	50	25	1.0	1.0	1.0	1.0	0.464
15	1650	400	60	−200	0.6625	50	25	1.0	1.0	1.0	1.0	0.672
16	1650	400	200	−200	0.8500	50	25	1.0	1.0	1.0	1.0	0.512
17	2000	400	30	−200	0.3866	50	25	1.0	1.0	1.0	1.0	0.192

Table 1: Parameter survey and ignition length results

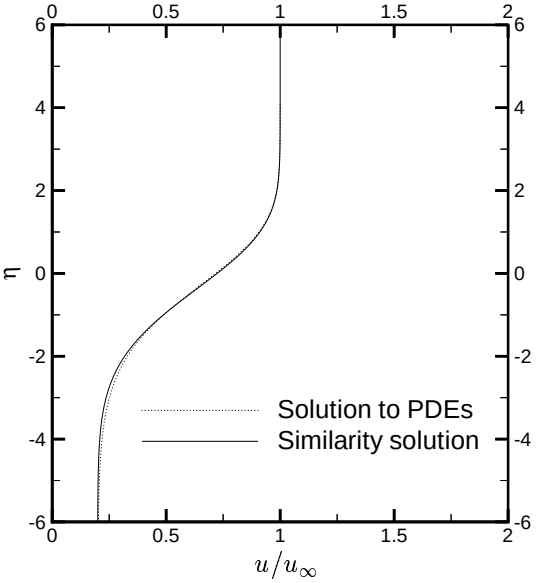

Figure 1: u/u_∞ vs. η for non-reacting similar case $K = 5$ and $\beta_M = 1$. The PDE solutions are at $x = 1.53$, 2.89, and 4.76 mm corresponding to $\overline{\xi} = 1$, 2, and 3, respectively.

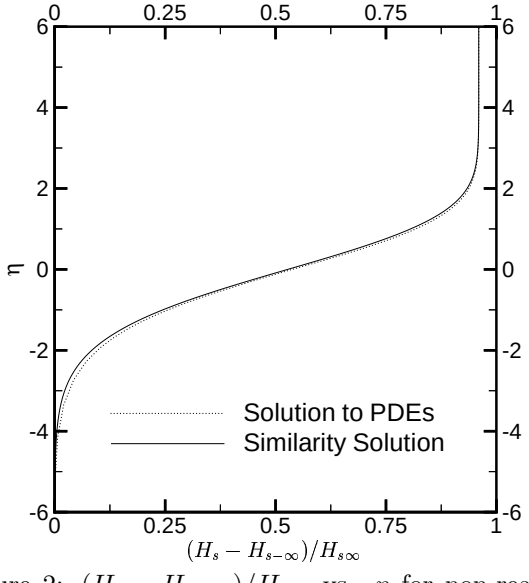

Figure 2: $(H_s - H_{s-\infty})/H_{s\infty}$ vs. η for non-reacting similar case $K = 5$ and $\beta_M = 1$. The PDE solutions are at $x = 1.53$, 2.89, and 4.76 mm corresponding to $\overline{\xi} = 1$, 2, and 3, respectively.

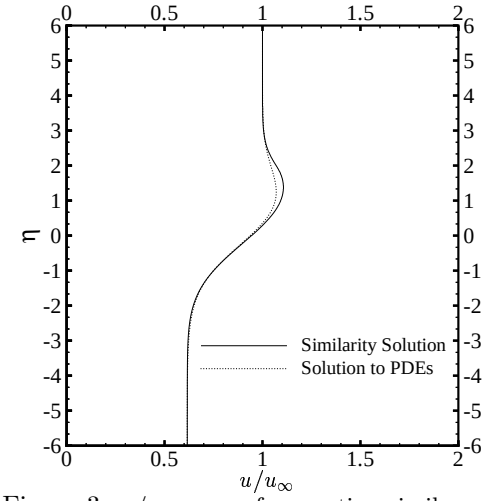

Figure 3: u/u_∞ vs. η for reacting similar case $K = 1.623$ and $\beta_M = 2$. The PDE solutions are at $x = 3.16$, 4.89, and 6.02 mm corresponding to $\overline{\xi} = 2$, 3, and 4, respectively.

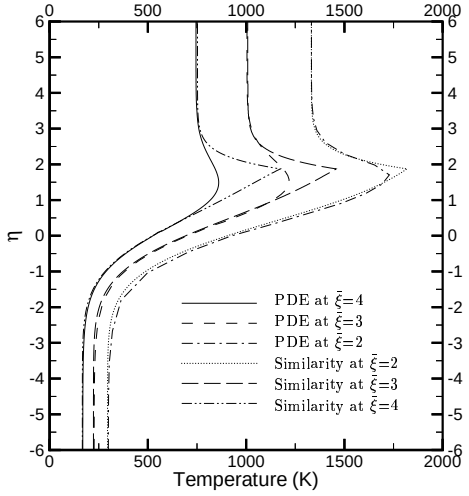

Figure 4: Temperature vs. η for reacting similar case $K = 1.623$ and $\beta_M = 2$. The PDE solutions are at $x = 3.16$, 4.89, and 6.02 mm corresponding to $\overline{\xi} = 2$, 3, and 4, respectively.

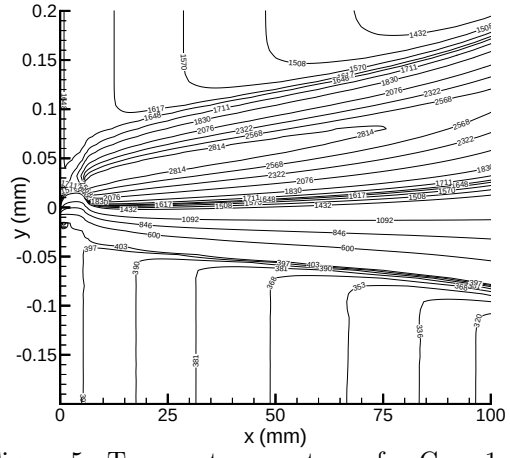

Figure 5: Temperature contours for Case 1 (the base case).

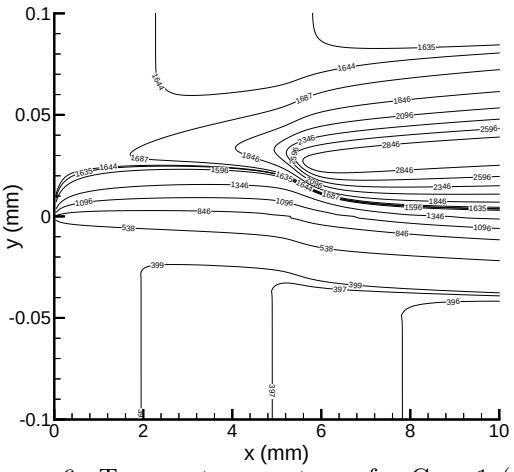

Figure 6: Temperature contours for Case 1 (the base case).

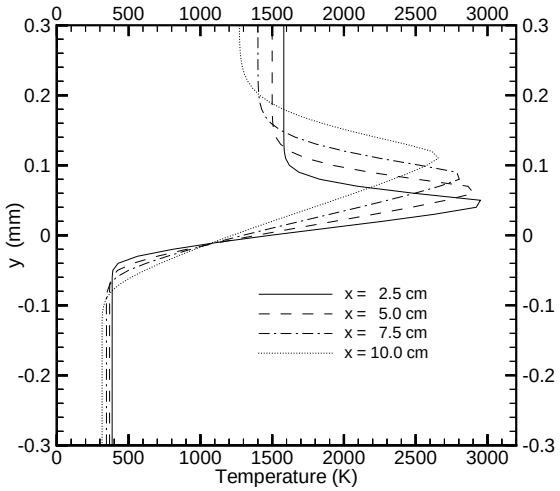

Figure 7: Temperature versus y at different x positions for Case 1 (the base case).

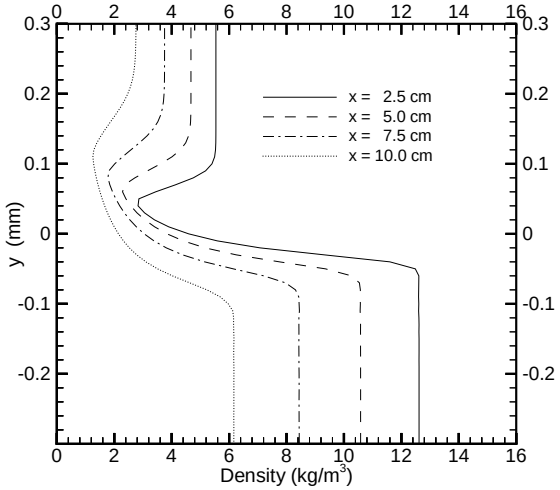

Figure 8: Density versus y for Case 1 (the base case).

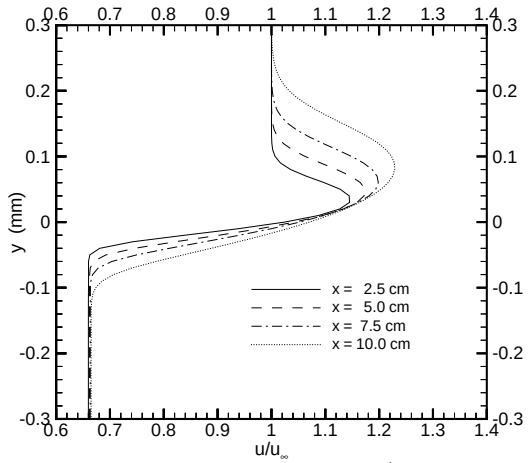

Figure 9: Dimensionless velocity u/u_∞ versus y at different x positions for Case 1 (the base case).

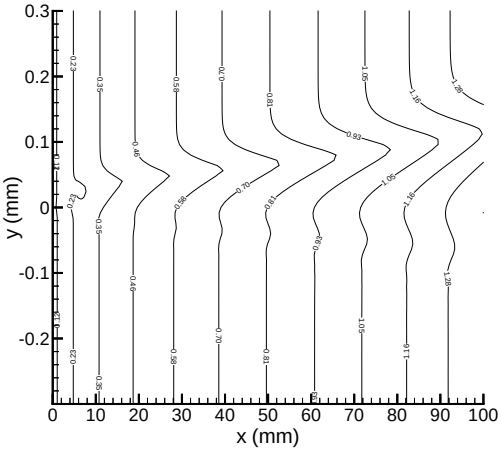

Figure 12: Mach number contours for Case 1 (the base case).

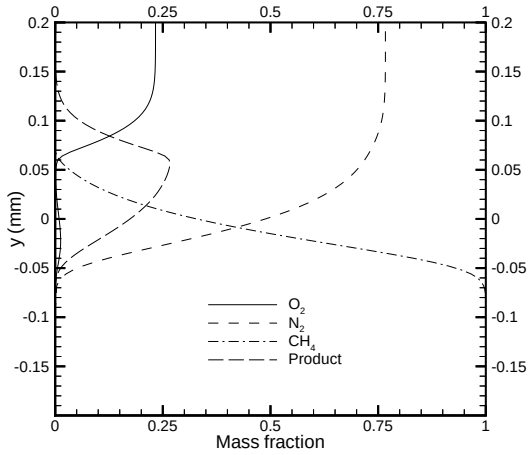

Figure 10: Mass fraction versus y at $x = 10$ cm for Case 1 (the base case).

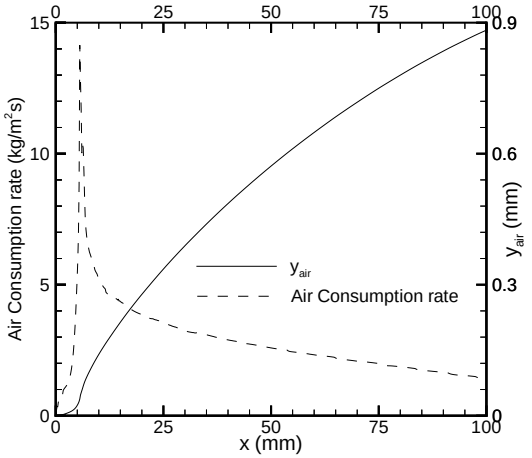

Figure 13: . y_{air} and air consumption rate for Case 1 (the base case).

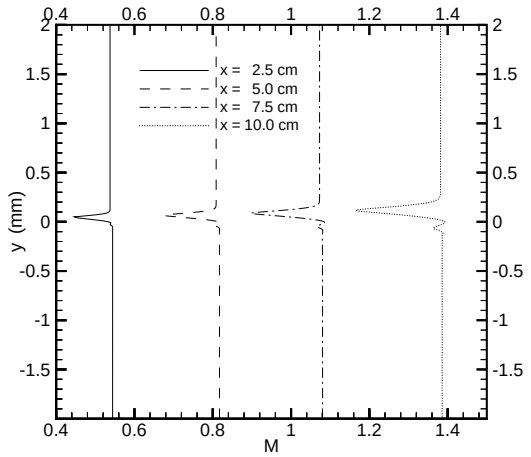

Figure 11: Mach number versus y at different x positions for Case 1 (the base case).

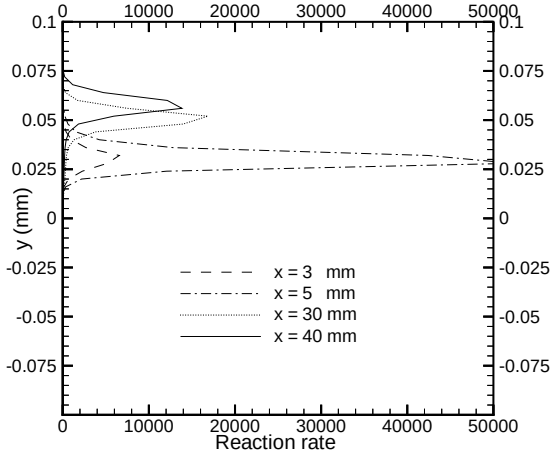

Figure 14: Reaction rate versus y at different x positions for Case 1 (the base case).

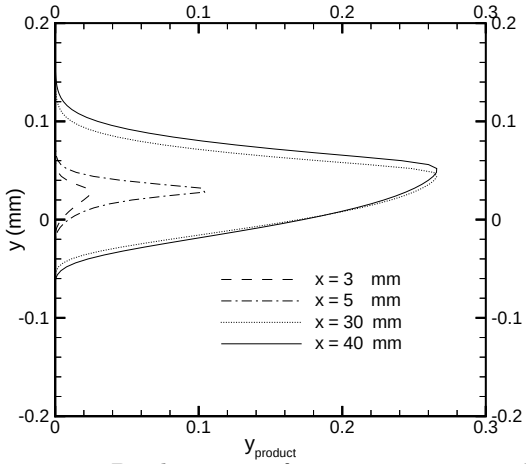

Figure 15: Product mass fraction versus y at different x positions for Case 1 (the base case).

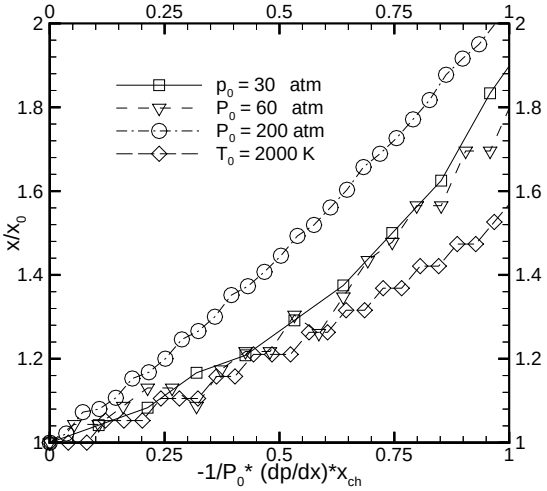

Figure 18: Dimensionless ignition distance vs. dimensionless ignition parameter.

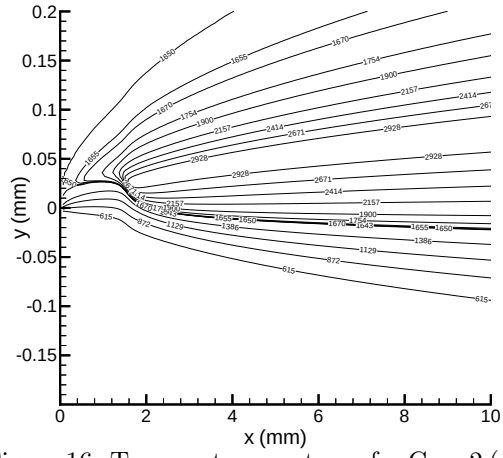

Figure 16: Temperature contours for Case 2 ($dp/dx = 0$ atm).

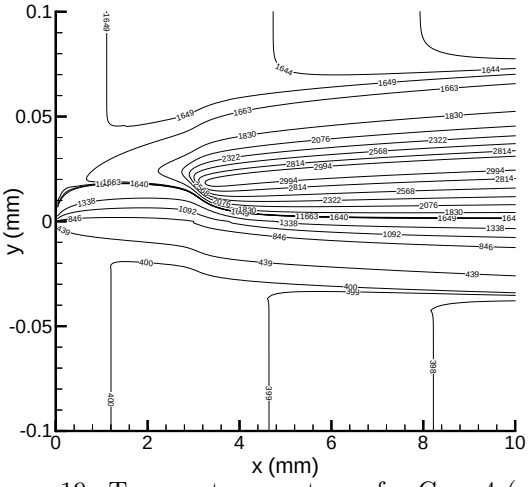

Figure 19: Temperature contours for Case 4 ($p_0 = 60$ atm).

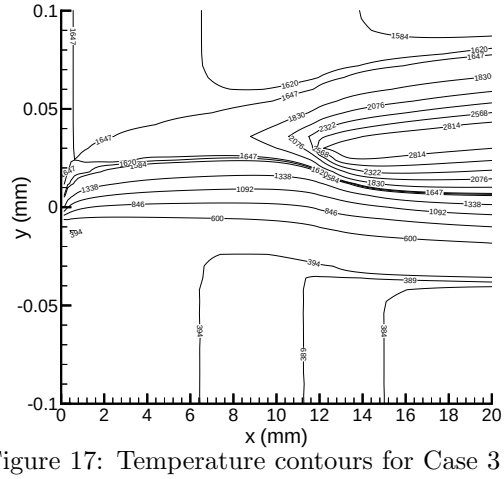

Figure 17: Temperature contours for Case 3 ($dp/dx = -350$ atm).

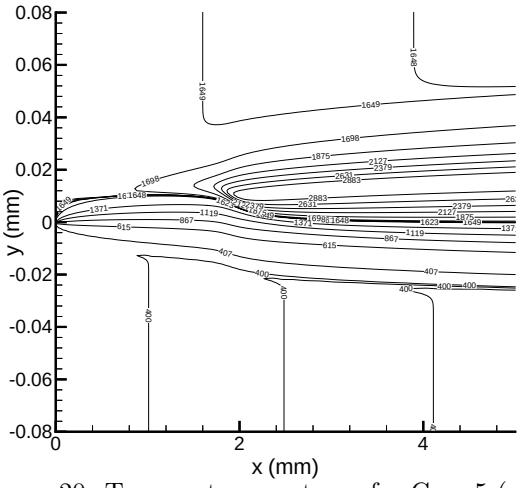

Figure 20: Temperature contours for Case 5 ($p_0 = 200$ atm).

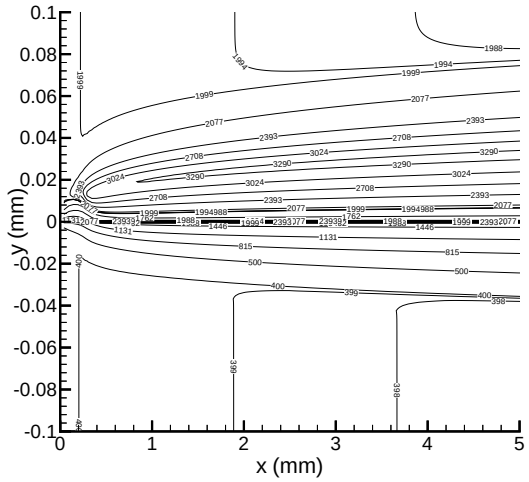

Figure 21: Temperature contours for Case 6 (T_{air} = 2000 K).

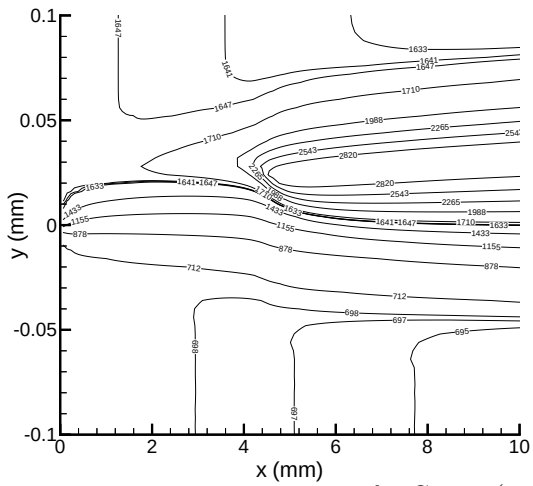

Figure 22: Temperature contours for Case 7 (T_F = 700 K).

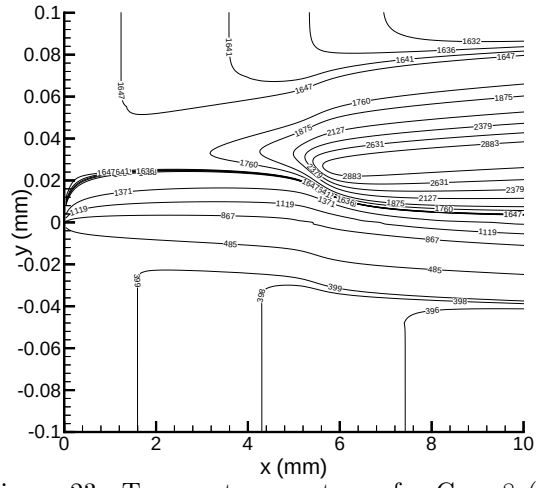

Figure 23: Temperature contours for Case 8 (u_{air} = 100 m/s).

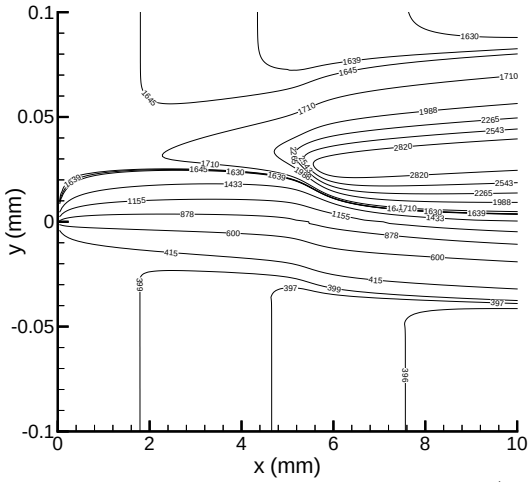

Figure 24: Temperature contours for Case 9 (u_F = 100 m/s).

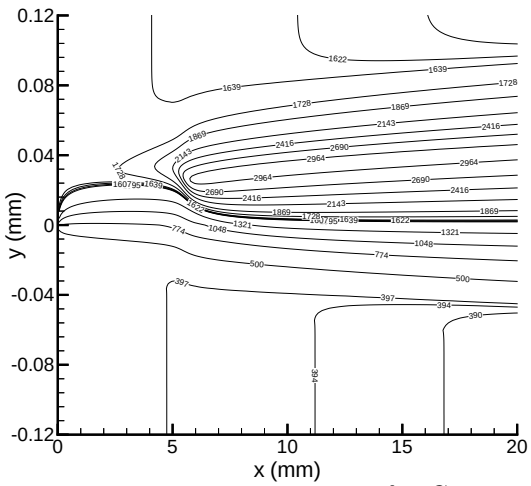

Figure 25: Temperature contours for Case 10 (Pr = 0.9).

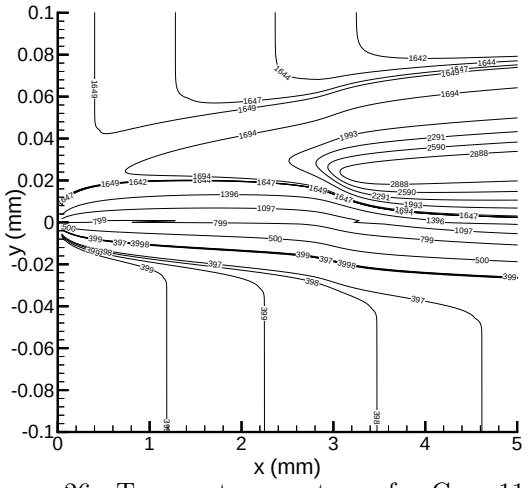

Figure 26: Temperature contours for Case 11 (Sc = 0.9).

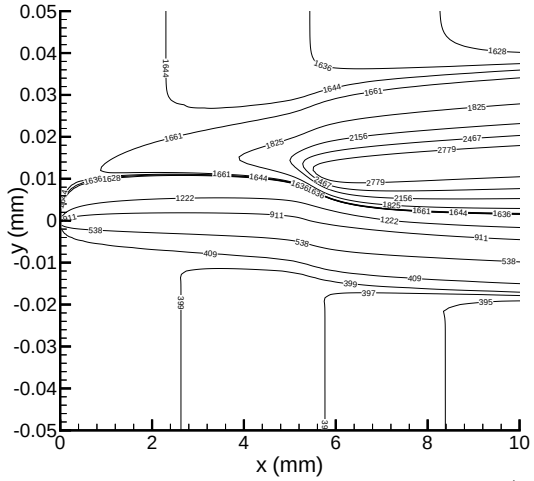

Figure 27: Temperature contours for Case 12 (decrease the viscosity coefficient μ by a factor of 5).

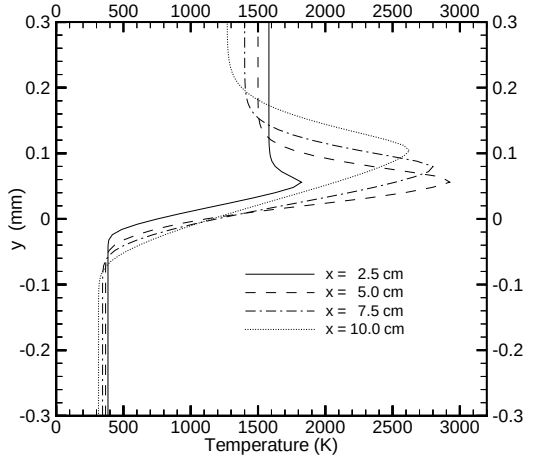

Figure 28: Temperature vs. y at different x positions for Case 13 (decrease the chemical reaction rate by a factor of 10).

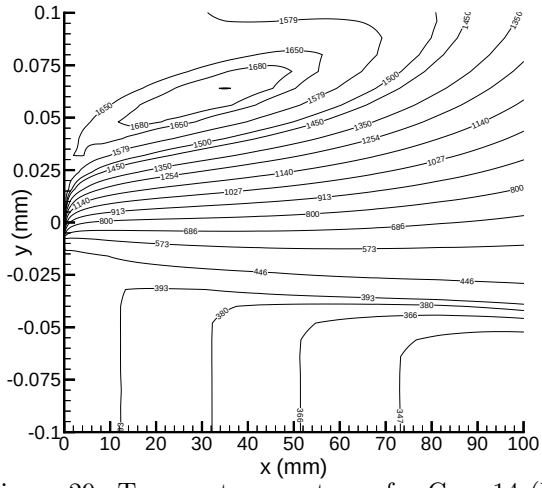

Figure 29: Temperature contours for Case 14 ($Y_{air} = 0.5848$)

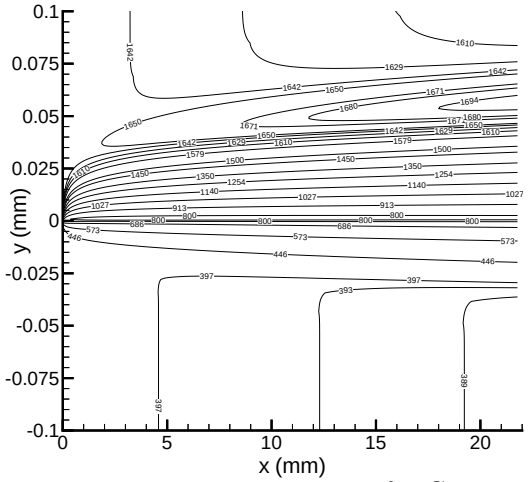

Figure 30: Temperature contours for Case 14 ($Y_{air} = 0.5848$).

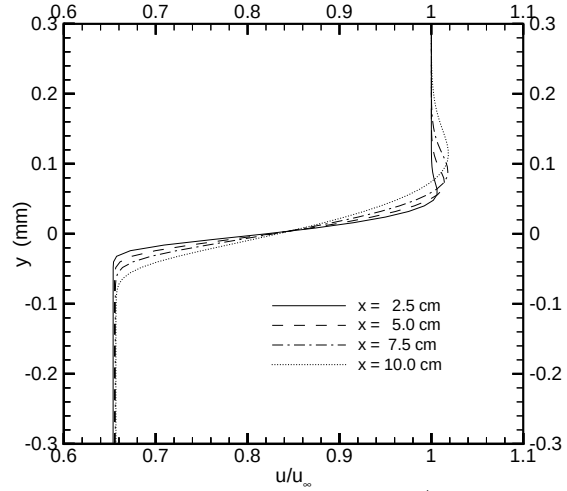

Figure 31: Dimensionless velocity u/u_∞ versus y at different x positions for Case 14 ($Y_{air} = 0.5848$).

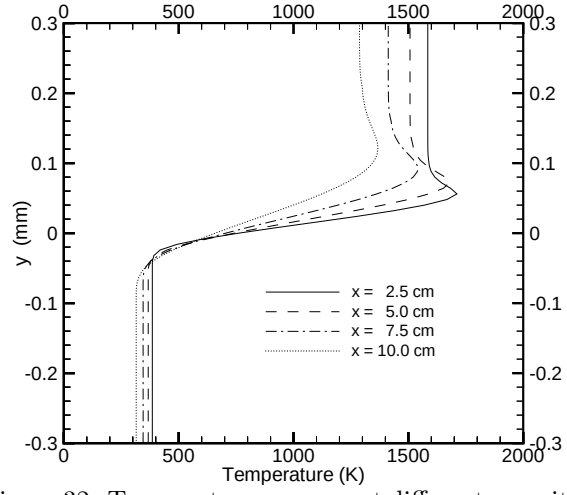

Figure 32: Temperature versus y at different x positions for Case 14 ($Y_{air} = 0.5848$).

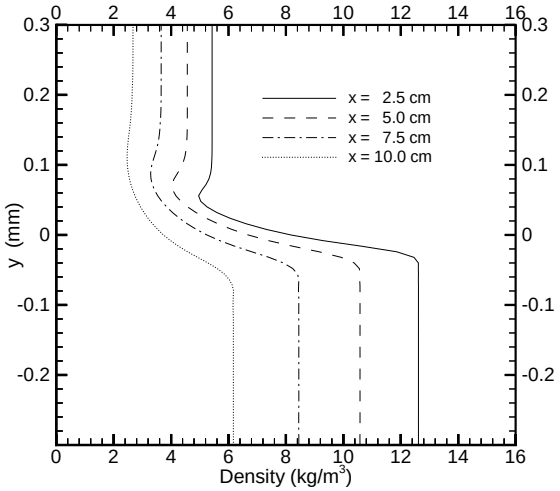

Figure 33: Density versus y at different x positions for Case 14 ($Y_{air} = 0.5848$).

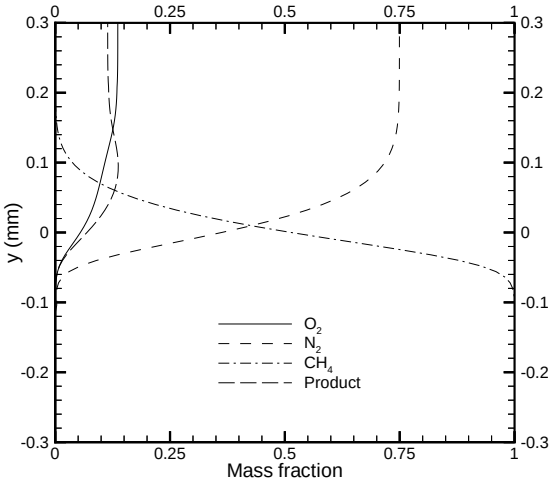

Figure 34: Mass fraction versus y at $x = 10$ cm for Case 14 ($Y_{air} = 0.5848$).

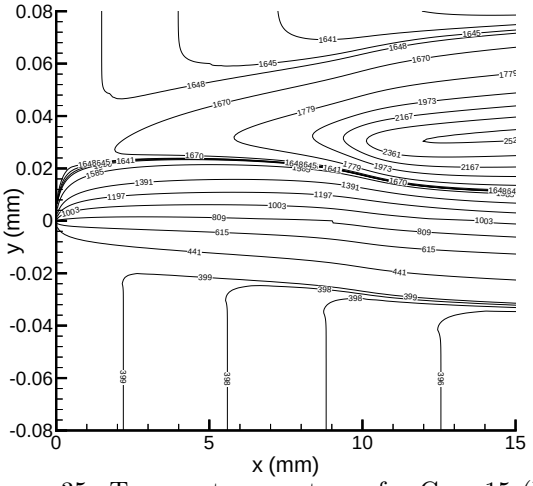

Figure 35: Temperature contours for Case 15 ($Y_{air} = 0.6625$, $p_0 = 60$ atm).

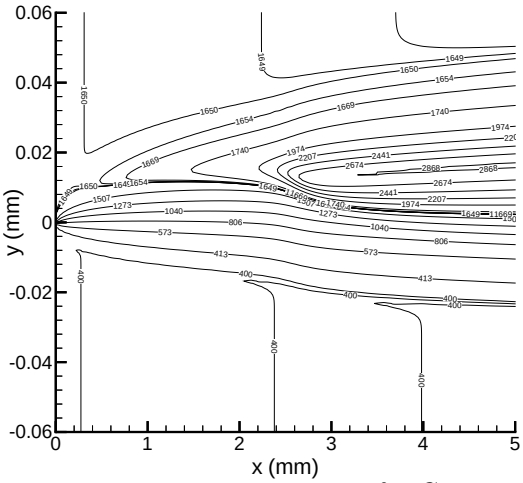

Figure 36: Temperature contours for Case 16 ($Y_{air} = 0.8500$, $p_0 = 200$ atm).

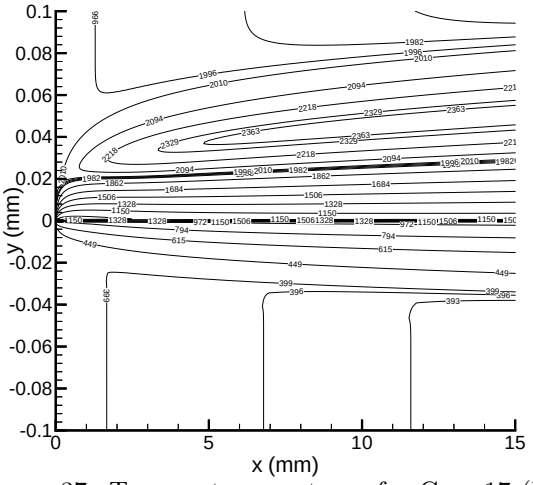

Figure 37: Temperature contours for Case 17 ($Y_{air} = 0.5848$, $T_0 = 2000$ K).